American Mineralogist, Volume 91, pages 489–502, 2006

Structural model for the biogenic Mn oxide produced by *Pseudomonas putida*

MARIO VILLALOBOS,[1,3,*] BRUNO LANSON,[2] ALAIN MANCEAU,[2] BRANDY TONER,[3] AND GARRISON SPOSITO[3]

[1]Environmental Bio-Geochemistry Group, LAFQA, Instituto de Geografía, National Autonomous University of Mexico (UNAM), Circuito Exterior, Ciudad Universitaria, Mexico, Coyoacán, 04510, D.F., Mexico
[2]Environmental Geochemistry Group, LGIT, Maison des Géosciences, BP53, University of Grenoble—CNRS, 38041 Grenoble Cedex 9, France
[3]Division of Ecosystem Sciences, University of California at Berkeley, Berkeley, California 94720-3114, U.S.A.

ABSTRACT

X-ray diffraction (XRD) and Mn K-edge extended X-ray absorption fine structure (EXAFS) spectroscopy were combined to elaborate a structural model for phyllomanganates (layer-type Mn oxides) lacking 3D ordering (turbostratic stacking). These techniques were applied to a sample produced by a common soil and freshwater bacterium (*Pseudomonas putida*), and to two synthetic analogs, δ-MnO_2 and acid birnessite, obtained by the reduction of potassium permanganate with $MnCl_2$ and HCl, respectively. To interpret the diffraction and spectroscopic data, we applied an XRD simulation technique utilized previously for well-crystallized birnessite varieties, complementing this approach with single-scattering-path simulations of the Mn K-edge EXAFS spectra. Our structural analyses revealed that all three Mn oxides have an hexagonal layer symmetry with layers comprising edge-sharing $Mn^{4+}O_6$ octahedra and cation vacancies, but no layer $Mn^{3+}O_6$ octahedra. The proportion of cation vacancies in the layers ranged from 6 to 17%, these vacancies being charge-compensated in the interlayer by protons, alkali metals, and Mn atoms, in amounts that vary with the phyllomanganate species and synthesis medium. Both vacancies and interlayer Mn were most abundant in the biogenic oxide. The diffracting crystallites contained three to six randomly stacked layers and have coherent scattering domains of 19–42 Å in the **c*** direction, and of 60–85 Å in the **a-b** plane. Thus, the Mn oxides investigated here are nanoparticles that bear significant permanent structural charge resulting from cation layer vacancies and variable surface charge from unsaturated O atoms at layer edges.

Keywords: Geomicrobiology, *Pseudomonas putida*, Mn oxide, XAS, biogenic Mn oxide, XRD data, crystal structure, new minerals

INTRODUCTION

Manganese 2+ oxidation occurs primarily through biological mediation in the oxic and oxic/anoxic transition zone of aqueous environments (Tipping et al. 1984; Nealson et al. 1988; Tebo 1991; Ghiorse and Ehrlich 1992; Bartlett and James 1993; Wehrli et al. 1995; Tebo et al. 1997; Harvey and Fuller 1998; Tebo and He 1999; Marble et al. 1999; Morgan 2000; Kay et al. 2001). The oxidation products are mainly insoluble Mn^{4+} oxides of the birnessite family (i.e., hydrous phyllomanganates) comprising edge-sharing MnO_6 octahedra with high negative permanent structural charge, due principally to vacant cation layer sites, and correspondingly high cation sorption capacities (Chukhrov et al. 1985; Strobel et al. 1987; Drits et al. 1997; Silvester et al. 1997; Lanson et al. 2000; Bilinski et al. 2002). Todorokite, a Mn oxide with tunnel structure, has also been found associated with birnessites in natural settings, but, since the latter are believed to be precursors to formation of the former (Golden et al. 1987; Shen et al. 1993; Tian et al. 1997; Ching et al. 1999; Luo et al. 1999; Feng et al. 2001), todorokite is probably not a direct product of microbial oxidation.

Natural Mn oxides often are poorly crystalline solids (Tipping et al. 1984; Friedl et al. 1997; McKeown and Post 2001; Bilinski et al. 2002; Manceau et al. 2003, 2004), and few structural investigations of them have been performed (Chukhrov et al. 1985, 1989; Manceau et al. 1992; Gorshkov et al. 1992). Mineralogical techniques that rely on the presence of long-range order, such as X-ray and electron diffraction, have been applied mainly to synthetic analogs of natural birnessites, most often with an enhanced three-dimensional (3D) ordering (Holland and Walker 1996; Drits et al. 1997; Silvester et al. 1997; Lanson et al. 2000, 2002a; Post et al. 2002; Jurgensen et al. 2004). These techniques have revealed the presence of two layer symmetries, orthogonal ($a > b\sqrt{3}$) as in triclinic Na-bearing birnessite (Lanson et al. 2002), hereafter referred to as NaBi, and hexagonal ($a = b\sqrt{3}$) as in H-bearing birnessite (Lanson et al. 2000), hereafter referred to as HBi, depending on the predominant origin of the layer charge (Mn^{3+} for Mn^{4+} substitution, or vacant Mn^{4+} sites within the octahedral sheet, respectively). HBi is formed under acidic pH conditions (Silvester et al. 1997). It has the hexagonal unit-cell parameters a = 4.940 Å, $b = a/\sqrt{3}$ = 2.852 Å, c = 7.235 Å, $\alpha = \beta = \gamma = 90°$, with 0.833 Mn ions and 0.167 cation vacancies per layer octahedron, and 0.167 interlayer $Mn^{2+,3+}$ ions located above or below layer vacancies in a triple-corner sharing configuration. The vacancies are long-range ordered, in that they appear in every third row of Mn cations along [100], with half of the Mn sites along these rows

* E-mail: marvilla@igg.unam.mx

being vacant (Drits et al. 1997). Water molecules associated with interlayer Mn cations provide for strong hydrogen bonds between the layers (Lanson et al. 2000).

Villalobos et al. (2003) characterized a set of analogs of natural birnessites showing a limited 3D ordering, including a biogenic Mn oxide produced in culture by a common soil and freshwater bacterium, *Pseudomonas putida*. Based on comparison of their layer symmetry, Mn oxidation numbers, and other physicochemical properties, all of the Mn oxides investigated appeared to be more structurally related to hexagonal HBi than to the triclinic NaBi variety. Also, the biogenic Mn oxide was concluded to have reactive and structural properties intermediate between those of the synthetic **c**-disordered phyllomanganates δ-MnO_2 and acid birnessite, which are formed through the reduction of permanganate with $MnCl_2$ or HCl, respectively. More recently, Jurgensen et al. (2004) studied the structure of the Mn oxide produced by another bacterium species (*Leptothrix discophora*) by X-ray absorption fine structure (XAFS) spectroscopy and X-ray diffraction (XRD). They found that this compound consists of single octahedral-layer microcrystals composed of Mn^{4+}, Mn^{3+}, and Mn^{2+} similarly to triclinic NaBi. They also identified the possible location of some Mn octahedra in corner-sharing configuration with those from the layer plane, as in HBi.

The birnessite samples previously studied by Villalobos et al. (2003) appear to have simple layer structures made up almost entirely of Mn^{4+} octahedra, their complexity arising from the presence of layer vacancies and lack of 3D ordering. In the present paper, we extend our previous work with a detailed structural investigation of the same samples using quantitative XRD and extended XAFS (EXAFS) spectroscopy. To interpret the XRD data, we applied a simulation technique utilized previously for birnessites with an enhanced 3D ordering (Manceau et al. 1997; Drits et al. 1998a; Lanson et al. 2000, 2002a, 2002b), complementing this approach with single-scattering-path analyses of Mn *K*-edge EXAFS spectra.

Experimental methods

Synthesis and characterization of Mn oxide samples

The biogenic Mn oxide and its two synthetic analogs were prepared using methods described in Villalobos et al. (2003). Briefly, the biogenic Mn oxide was produced in cultures of *Pseudomonas putida* strain MnB1 provided by Dr. B.M. Tebo (Scripps Institution of Oceanography). Bacteria were grown at 27 °C to the stationary phase of growth in a liquid suspension rich in nutrients and in the presence (or absence, for a cell control sample) of total $[Mn^{2+}] = 1.0$ mM. A sample of the biogenic oxide was cleaned of organic material by gradual iterative oxidation using 0.2% NaOCl reagent, taking care not to oxidize Mn^{4+} or Mn^{3+} in the sample. δ-MnO_2 was prepared using a "redox" method with stoichiometric amounts of $KMnO_4$ and $MnCl_2$ reagents (Catts and Langmuir 1986; Mandernack et al. 1995; Luo and Suib 1997; Luo et al. 2000). Physicochemical characterization of the sample (Villalobos et al. 2003) indicated a composition exclusively of Mn^{4+} and a highly pH-dependent cation sorption capacity. Acid birnessite was prepared by reducing $KMnO_4$ with concentrated HCl at boiling temperature (McKenzie 1971). The solids were oven-dried overnight at 70 °C, except for acid birnessite, which was freeze-dried, and a sample of uncleaned biogenic oxide, which was washed, centrifuged, and left as a wet paste for in-situ EXAFS spectroscopy.

Thermogravimetric analyses (TGA) were performed to determine the water content on ca. 20 mg of the dried samples except for the uncleaned biogenic oxide. The weight loss was measured by heating the samples on a Pt tray from room temperature to ca. 250 °C at a rate of 10 °C/min (SDT 2960 apparatus from TA Instruments). Alumina powder was used as reference material for weight loss calibrations. Two peaks were obtained in plots of weight/temperature differentials vs. temperature for all samples. They were decomposed using Galactic Grams 32 (vol. 6) software to determine the fractions of loosely bound (removed at <80 °C) and strongly sorbed water (released between 80–250 °C—H_2O content in Table 1), but excluding structural water bound to interlayer Mn cations. Duplicate analyses per sample were performed, and the results obtained were used to constrain the water contents in the XRD simulations.

X-ray diffraction

Dry samples were crushed in an agate mortar, and powder XRD patterns (Cu*K*α radiation, λ = 1.5418 Å) were collected with a Bruker D5000 powder diffractometer equipped with a Kevex Si(Li) solid-state detector. Intensities were measured at 0.04 °2θ intervals with 40 s counting time per step.

Simulations of XRD patterns were performed following the trial-and-error procedure developed by Drits and Tchoubar (1990), and applied previously to both natural and synthetic birnessites (Chukhrov et al. 1985; Manceau et al. 1997; Drits et al. 1998a; Lanson et al. 2000, 2002a, 2002b). Details on the programs used to simulate XRD patterns and on the fitting procedure are given by Drits and Tchoubar (1990), Drits et al. (1998a), and Plançon (2002). As the main features of XRD profiles recorded for the three samples resemble those reported by Drits et al. (1997) for turbostratic birnessite, the experimental patterns were divided for the simulations in two angular domains containing different families of reflections. In the low-angle region (5–30 °2θ Cu*K*α—*d*-spacing >10 to 3.0 Å), 00*l* reflections were calculated to assess the validity of the lamellar structure proposed by Villalobos et al. (2003) for the synthetic oxides. In addition, the simulation of 00*l* reflections allowed quantification of the extent of coherent scattering domains (CSDs) along the axis perpendicular to the **a-b** plane (**c*** axis) using a lognormal distribution of CSD sizes parameterized by an average number of layers (N_{Av}, Drits et al. 1998b). In the high-angle range (32–75 °2θ Cu*K*α—*d*-spacing 2.80–1.27 Å), the 20*l*,11*l* and the 02*l*, 31*l* reflections (Miller indexing based on a C-centered unit cell) were calculated to determine the structure of both the octahedral layer and the interlayer region (atomic coordinates and occupancies of the different sites). CSDs in the **a-b** plane were assumed to have a disk-like shape whose average radius was constrained by fitting the first of the two high-angle maxima. For all samples, the background was assumed to decrease linearly over the angular range considered. The average Mn oxidation number along with the alkali metal and structural water content of the samples were used to constrain initial assumptions about the stoichiometry of interlayer species in the simulations. Quality of fit was assessed over the 34–75 °2θ Cu*K*α range assuming the commonly employed R_{wp} factor, and comparing it to the statistical error associated with measured intensities (R_{Exp}) (Howard and Preston 1989).

EXAFS spectroscopy

Manganese *K*-edge EXAFS spectra were measured at room temperature on wiggler beamline 4-3 at the Stanford Synchrotron Radiation Laboratory in transmission mode. A Si(220) crystal pair was used to create monochromatic X-rays and a Pt-coated mirror was used to reject harmonic X-rays. A 1 mm vertical entrance slit located 17.2 m from the source was used to improve the energy resolution by reducing the beam divergence on the monochromator. Dry Mn oxide samples were mixed with $LiCO_3$ [Mn oxide:$LiCO_3$ (w/w) ≈ 1:10], to ensure an absorbance of the edge jump of 1 to 1.5, then mounted on 1 mm thick Teflon holders in 25 × 3 mm slots. Raw biogenic oxide with cellular material was centrifuged and mounted directly as wet paste into these holders. Samples were held in place with Kapton tape X-ray windows. Spectra were acquired over the energy range 6400 to 7400 eV, with typically two to three runs per sample performed, each run taking approximately 30 min. Either a permanganate solid (Mn^{7+}) (absorption edge jump at 6543 eV set at the maximum of the first derivative of the edge), or a Mn metal foil (absorption edge jump at 6539 eV) were used to calibrate the monochromator before every sample

Table 1. Physicochemical properties of the Mn oxides investigated

Mn oxide	H_2O content (%w/w) (± 0.02)	Average Mn oxidation number (± 0.02) †	Structural Alc*/Mn_{tot} (mol%)†
Biogenic‡	10.0	3.90 ± 0.05	(pH 8.1) 16.7 ± 0.3
Acid Birnessite	7.5	3.96	(pH 5.6) 20.4 ± 0.8
δ-MnO_2	15.8	4.02	(pH 8.1) 25.3 ± 0.1

* Alc refers to the alkaline counterion, which is K^+ for acid birnessite and Na^+ for the others.
† From Villalobos et al. (2003).
‡ From *Pseudomonas putida*.

run. No beam-induced changes in Mn oxidation state were observed.

The EXAFS data analysis was performed in the single-scattering approximation using homemade software for data normalization and Fourier transformation, and WinXAS (Ressler 1998) for spectral simulations. Fourier transformations were done on the entire $k^3\chi(k)$ curves shown in the Results section with a Kaiser-Bessel window ($\tau = 3$). Transformation from reciprocal (k) to real (R) space produces radial structure functions (RSFs) with peaks corresponding to average absorber-backscatterer distances, but deviating from the true R distance by ΔR due to a phase shift. Spectral simulations were performed on Fourier-filtered data using Mn-O and Mn-Mn phase shift and amplitude functions calculated with FEFF v. 7 (Zabinsky et al. 1995) for the λ-MnO_2 reference (Thackeray et al. 1993). The Mn-O and Mn-Mn FEFF files were tested on the spectrum of the reference, and good agreement was found between EXAFS and crystallographic values. ΔE, the difference between the experimental (taken to be the half-edge jump point) and theoretical origins for the energy scale (E), was treated as a single adjustable parameter for all sets of backscattering atoms, and S_0^2, the amplitude reduction factor, was calibrated using λ-MnO_2. Since the EXAFS analysis in the present work is limited to single-scattering-path calculations, any interpretation of long distance Mn-Mn pairs shells ($R + \Delta R > 3.5$ Å), which requires full multiple-scattering calculations, is semi-quantitative. Below this distance, multiple scattering (MS) contributions are negligible (see Fig. 15 of Manceau et al. 1998).

RESULTS AND DISCUSSION

XRD patterns

Figure 1 shows a maximum of four major XRD peaks for the Mn oxide samples studied, whose positions and relative intensities closely resemble those reported by Drits et al. (1997) for turbostratic birnessite. From this positive comparison it is possible to hypothesize that the two peaks occurring at ~7.3–8.0 and 3.6–3.8 Å correspond to 001 and 002 basal reflections, although they do not strictly define a rational series. In addition, these reflections are significantly shifted as compared to the positions of 00*l* reflections commonly reported for birnessite samples. The two peaks observed at higher angles (2.42–2.44 and 1.41–1.42 Å) likely correspond to 20,11 and 02,31 bands, respectively, choosing a C-centered layer cell. The ratio of the d values of the two bands (1.720–1.725) is close to the $1.732 = \sqrt{3}$ value expected for layers having a hexagonal symmetry. These bands do not show significant modulations of the *hkl* reflections, and instead exhibit a strong asymmetry on their high-angle side.

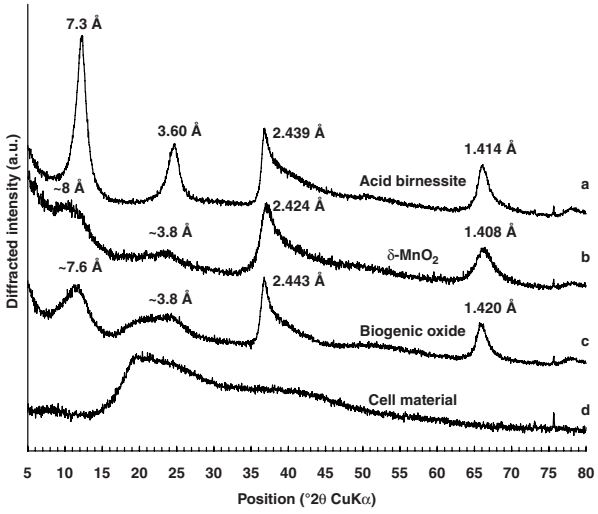

FIGURE 1. Experimental XRD patterns of the Mn oxide samples. (**a**) acid birnessite, (**b**) δ-MnO_2, (**c**) biogenic oxide with cell material, (**d**) cell material without the biogenic oxide.

This profile shape is characteristic of lamellar compounds with a turbostratic stacking, i.e., lacking well-defined displacement/rotation between successive layers (Brindley 1980). A broad "hump" is however visible at ca. 50–55 °2θ Cu$K\alpha$ for all three samples (Fig. 1). In comparison to the acid birnessite (Fig. 1a), the first two maxima at ~8 and 3.8 Å for δ-MnO_2 are broadened (Fig. 1b), and also significantly shifted relative to their ideal positions for a «7 Å» lamellar compound. The broadening of the basal reflections of δ-MnO_2 extends to the 20,11 and 02,31 bands, and the broad "hump" between 50 and 55 °2θ Cu$K\alpha$ has a different shape from that of the acid birnessite pattern. The two low-angle maxima of the pattern for the biogenic oxide are at ~7.6 and 3.8 Å, and have a shape intermediate between those of the two previous samples (Fig. 1c). The biogenic oxide pattern exhibits an additional shoulder on the low-angle side of the 3.8 Å maximum. This shoulder arises from the contribution of dead cells to the diffracted intensity, as shown on the XRD pattern from the bacteria alone (Fig. 1d). The admixture of bacterial cells does not modify significantly the pattern from the biogenic oxide component in the high-angle region. The two 20,11 and 02,31 bands are still observed for the biogenic oxide, but the high-angle tail of the former is less pronounced than in the two other samples, and the hump is slightly shifted to higher 2θ values.

Simulations of the low-angle region (5–30 °2θ Cu$K\alpha$)

One objective of these simulations was to verify if the observed non-rationality and the significant positional shift of the two diffraction maxima observed in this low-angle range was related to the small dimensions of the CSDs along the **c*** direction as described by Drits and Tchoubar (1990) for layer silicates. Calculations were performed assuming a lamellar structure for all three oxides considered. Elementary birnessite layers consist of the sheet of Mn octahedra itself, which possibly contains vacant layer sites, and of associated interlayer species, which include interlayer Mn and alkali cations, and coordinated H_2O molecules (see Eq. 1 below). Atomic coordinates along the **c*** direction were equal to those determined from the analysis of *hk* bands. Upon fixing these values, the amplitude, width, and position of the experimental diffraction peaks in this region essentially depend on the size of the CSDs along **c*** and, therefore, on the number of layers in the diffracting crystallites.

Although the fits to the experimental data are not perfect, the main features of the diffraction patterns were fairly reproduced by the simulations (Fig. 2). In particular, for all three samples the calculated positions, widths, and relative intensities were similar to the experimental data, thus providing strong support for the assumed lamellar structure of the unknowns (Villalobos et al. 2003). For the biogenic sample, the scattering from dead bacterial cells was not included in the calculation and, hence, only the high-angle contribution of the 002 peak was reproduced. The average sizes of the CSDs estimated from the models equal 2.6 layers (~1.9 nm) for δ-MnO_2, 2.8 layers (~2.0 nm) for the biogenic oxide, and 5.8 layers (~4.2 nm) for the acid birnessite (Table 2).

Simulations of the high-angle region (>30 °2θ Cu$K\alpha$)

The successful simulation of the low-angle peaks supports our indexing of the high-angle reflections as 20,11 and 02,31

bands. As compared to equivalent reflections for hydrous layer silicates (Manceau et al. 2000a, 2000b), the profiles of the 20,11 reflections are modulated and their shapes are different from one sample to another, indicating a variation of the structure factors, and hence of the sample structures. As will be shown below, these modulations can be used to determine both the layer and interlayer structures of the phyllomanganate samples despite the absence of any 3D ordering.

For all simulations the generic structural formula,

$$H_a(Na,K)_bH_2O_cMn_{tc}^{3+,2+}[Mn_d^{4+}, \square_c]O_2 \quad (1)$$

was assumed, where interlayer species are written to the left of the square brackets and tc refers to interlayer Mn in triple corner-sharing positions above or below cation vacancies (□) in the layer (enclosed in square brackets, except for the O atoms). The stoichiometric coefficients were calculated from the average Mn oxidation number and the alkali metal content determined previously (Villalobos et al. 2003), and from the water content determined by TGA (Table 1). Parameters refined in the XRD simulations include the unit-cell dimensions in the **a-b** plane, from the position of the two high-angle maxima, and the amount of vacant layer sites, the amount and position of interlayer Mn cations, the positions of interlayer alkali cations and of associated H_2O molecules, and the size of the CSDs in the **a-b** plane. All sample spectra were simulated assuming a hexagonal layer symmetry and choosing a C-centered unit cell with parameters $b = 2.838$ Å, $a = b\sqrt{3} = 4.916$ Å, $\gamma = 90°$, and a basal $d(001)$ distance of 7.20 Å. No parameters were used to define the layer-stacking mode, as layer stacking is random with W_R, the occurrence probability of random displacement/rotation between adjacent layers, being equal to 100%. Optimal parameters obtained from the simulations shown in Figure 3 are listed in Tables 2 and 3, and selected interatomic distances are reported in Table 4.

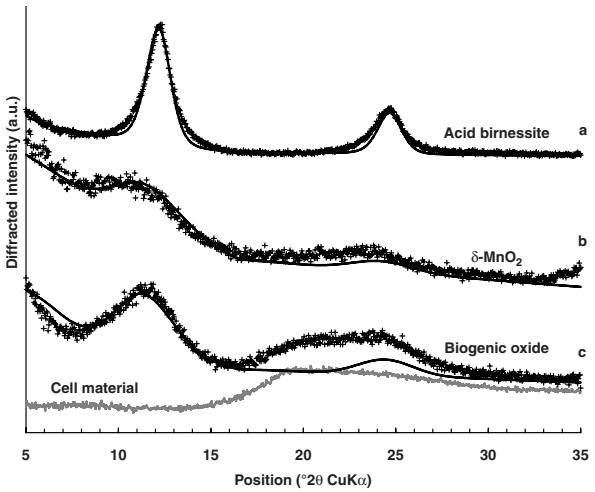

FIGURE 2. Comparison between experimental (plus sign symbols) and calculated (solid line) XRD patterns for the various Mn oxide samples. Structural parameters used for calculations are listed in Tables 2 and 3. Calculations are limited to the 00*l* reflections occurring below 35 °2θ Cu*K*α. (**a**) acid birnessite, (**b**) δ-MnO_2, (**c**) biogenic oxide with cell material. The lower gray trace in **c** is the experimental XRD pattern for cell material without the biogenic oxide.

δ-MnO_2. Since the average Mn oxidation number measured for this oxide is 4.0 (Table 1), the layer charge deficit was assumed to arise only from vacant layer sites. The optimal model had 6% octahedral vacancies, and did not contain interlayer Mn

TABLE 2. Optimum structural parameters used for the simulation of the three experimental X-ray diffraction profiles (cf. Figs. 2 and 3)

Atom	δ-MnO_2	Acid birnessite	Biogenic oxide
a (Å)	4.916	4.916	4.916
b (Å)	2.838	2.838	2.838
d(001) (Å)	7.20	7.20	7.20
Average CSD size (along the **c*** axis)	2.6	5.8	2.8
Average CSD size (in the **a-b** plane)	60	70	85

Notes: Optimal values were determined by trial-and-error fitting of the experimental XRD patterns. *a* and *b* parameters were determined from the simulation of the *hk* bands whereas the *c* parameter was estimated from the simulation of the 00*l* reflections. Coherent scattering domain (CSD) sizes along **c*** are expressed as number of layers, whereas the average radius of the CSDs in the **a-b** plane is expressed in Å. The latter values have been determined by fitting the 20,11 band.

TABLE 3A. Optimum structural parameters used for the simulation of δ-MnO_2 X-ray diffraction profile (cf. Fig. 3a)

Atom	*x*	*y*	ζ	Occ.	*x*	*y*	ζ	Occ.
Mn_{layer}	0	0	0	0.94	–	–	–	–
O_{layer}	0.333	0	1.00	1.00	–0.333	0	–1.00	1.00
$Mn_{interlayer}$	–	–	–	0.00	–	–	–	0.00
$H_2O_{interlayer}$	–	–	–	0.00	–	–	–	0.00
$Na_{interlayer}$	0.225	0	3.60	0.04	–0.225	0	–3.60	0.04
$Na_{interlayer}$	–0.1125	0.3375	3.60	0.04	–0.1125	–0.3375	3.60	0.04
$Na_{interlayer}$	0.1125	0.3375	–3.60	0.04	0.1125	–0.3375	–3.60	0.04
$H_2O_{interlayer}$	0.225	0	3.60	0.12	–0.225	0	–3.60	0.12
$H_2O_{interlayer}$	–0.1125	0.3375	3.60	0.12	–0.1125	–0.3375	3.60	0.12
$H_2O_{interlayer}$	0.1125	0.3375	–3.60	0.12	0.1125	–0.3375	–3.60	0.12

Notes: Optimal values were determined by trial-and-error fitting of the experimental XRD patterns. *x* and *y* coordinates are expressed as fractions of the *a* and *b* parameters, respectively. Coordinates along the **c*** axis, ζ, are expressed in Å to emphasize the thickness of layer and interlayer polyhedra. Un-refined thermal *B* factors are 0.5 for Mn_{layer}, 1.0 for O_{layer} and $Mn_{interlayer}$, and 1.5 for interlayer H_2O molecules associated with $Mn_{interlayer}$, and 2.0 for other interlayer species (alkali cations and H_2O molecules)

TABLE 3B. Optimum structural parameters used for the simulation of acid birnessite X-ray diffraction profile (cf. Fig. 3b)

Atom	*x*	*y*	ζ	Occ.	*x*	*y*	ζ	Occ.
Mn_{layer}	0	0	0	0.88	–	–	–	–
O_{layer}	0.333	0	1.00	1.00	–0.333	0	–1.00	1.00
$Mn_{interlayer}$	0	0	2.15	0.04	0	0	–2.15	0.04
$H_2O_{inter.}$	–0.333	0	3.35	0.12	0.333	0	–3.35	0.12
$K_{interlayer}$	–0.203	0	3.60	0.03	0.203	0	–3.60	0.03
$K_{interlayer}$	–0.4167	0.125	3.60	0.03	–0.4167	–0.125	3.60	0.03
$K_{interlayer}$	0.4167	0.125	–3.60	0.03	0.4167	–0.125	–3.60	0.03
$H_2O_{inter.}$	0.200	0	3.60	0.09	–0.200	0	–3.60	0.09
$H_2O_{inter.}$	–0.100	0.300	3.60	0.09	–0.100	–0.300	3.60	0.09
$H_2O_{inter.}$	0.100	0.300	–3.60	0.09	0.100	–0.300	–3.60	0.09

TABLE 3C. Optimum structural parameters used for the simulation of the biogenic oxide X-ray diffraction profile (cf. Fig. 3c)

Atom	*x*	*y*	ζ	Occ.	*x*	*y*	ζ	Occ.
Mn_{layer}	0	0	0	0.833	–	–	–	–
O_{layer}	0.333	0	1.00	1.00	–0.333	0	–1.00	1.00
$Mn_{interlayer}$	0	0	2.15	0.0833	0	0	–2.15	0.0833
$H_2O_{inter.}$	–0.333	0	3.35	0.25	0.333	0	–3.35	0.25
$Na_{interlayer}$	0.225	0	3.60	0.04	–0.225	0	–3.60	0.04
$Na_{interlayer}$	–0.1125	0.3375	3.60	0.04	–0.1125	–0.3375	3.60	0.04
$Na_{interlayer}$	0.1125	0.3375	–3.60	0.04	0.1125	–0.3375	–3.60	0.04
$H_2O_{inter.}$	0.225	0	3.60	0.12	–0.225	0	–3.60	0.12
$H_2O_{inter.}$	–0.1125	0.3375	3.60	0.12	–0.1125	–0.3375	3.60	0.12
$H_2O_{inter.}$	0.1125	0.3375	–3.60	0.12	0.1125	–0.3375	–3.60	0.12

(tc = 0). Accordingly, the layer charge deficit was compensated by interlayer Na, whose fraction was constrained to be four times the refined fraction of vacant layer sites. The amount of interlayer H_2O was assumed to be three times the amount of interlayer Na (Post and Veblen 1990), leading to a water content (12.7%) consistent with the TGA value (15.8%), although somewhat smaller. Thus, the structural formula corresponding to the optimum fit shown in Figure 3a (R_{WP} = 10.7%, R_{EXP} = 3.5%) is:

$$Na_{0.24}(H_2O)_{0.72}[Mn^{4+}_{0.94},\square_{0.06}]O_2 \quad (2)$$

The coordinates of Na and H_2O are (0.225, 0, 1/2), and equivalent positions (Table 3a and Fig. 4), and the distance between water molecules and nearest layer O atoms (O_{layer}) is 2.65 Å, which is favorable to the formation of strong H-bonds (Table 4).

Acid birnessite. The average Mn oxidation state of slightly lower than 4.0 (Table 1) suggests the occurrence of Mn^{3+} cations, most likely above/below vacant layer sites, since the layer has an hexagonal symmetry. Thus, the amounts and positions of interlayer Mn were optimized during the simulations, together with the amount of octahedral vacancies. The amount of interlayer H_2O was linked to that of alkali cations, as for the δ-MnO_2 simulation, and their positions were also optimized. The refined structural formula, which yielded the optimum match between the calculated scattering profile and data shown in Figure 3b (R_{WP} = 9.3%, R_{EXP} = 2.8%), is:

$$H_{0.06}K_{0.18}(H_2O)_{0.54}Mn^{3+}_{0.08}(H_2O)_{0.24}[Mn^{4+}_{0.88},\square_{0.12}]O_2 \quad (3)$$

This sample has a higher amount of vacant layer sites (0.12 per octahedron) than δ-MnO_2, and only two-thirds of the octahedral vacancies (0.08 per octahedron) are capped on one side by octahedrally coordinated interlayer Mn^{3+} cations (Fig. 4). The stoichiometric coefficient of Mn^{3+} is about half that of HBi (Lanson et al. 2000). The average Mn oxidation degree (3.92) determined by XRD agrees fairly well with the value determined by wet chemistry (3.96 ± 0.02, Villalobos et al. 2003), which provides confidence in the overall consistency of our structural approach. The remaining layer charge is balanced by interlayer K^+ cations and protons (0.18 and 0.06 per octahedron, respectively), the alkali metal content (K/Mn = 0.19) being consistent with the K/Mn molar ratio measured by wet chemistry (0.20 ± 0.008, Villalobos et al. 2003). The amount of structural water (9.6%) is consistent with the TGA value (7.5%, Table 1), although somewhat larger. The position of the water molecules (0.200, 0.0, 0.5—and equivalent positions; Table 3b) is close to that determined for δ-MnO_2 (0.225, 0.0, 0.5), and again leads to a short <H_2O-O_{layer}> distance (2.68 Å) that is favorable to the formation of strong H-bonds with O_{layer}. However, the assumption of a common position for K^+ and H_2O did not yield optimal fits to the XRD pattern (R_{wp} = 10.3%). Best agreement between calculation and experiment was obtained with K^+ at (–0.203, 0.0, 0.5) - and equivalent positions, which is above or below empty tridentate cavities of the layer surface at 2.97 Å from O_{layer}. K atoms are slightly shifted in the **a-b** plane from the center of the cavity in the direction of the nearest O_{layer}-O_{layer} edge of the Mn layer (Fig. 4). This position is close to that refined by Gaillot et al. (2003) (–0.229, 0.0, 0.5) for a birnessite single crystal having 11% octahedral vacancies, of which two thirds were capped on one side by Mn^{3+} cations. The similar layer and interlayer structures found in the disordered birnessite synthesized at room temperature, and in the single crystal form synthesized at 800 °C suggest common structural principles despite the differing conditions of formation of the two species.

TABLE 4. Typical inter-atomic distances calculated from the optimum atomic coordinates

Atomic pair	δ-MnO_2	Acid birnessite	Biogenic oxide
Mn_{layer}-O_{layer}	1.920 Å	1.920 Å	1.920 Å
$Mn_{inter.}$-O_{layer}	–	2.00 Å	2.00 Å
$Mn_{inter.}$-H_2O	–	2.03 Å	2.03 Å
*$AlC_{inter.}$-O_{layer}	2.65 Å	2.97 Å	2.65 Å
*AlC_{inter}-H_2O	2.838 Å	2.93 ×1 / 2.99 ×2 / 3.02 ×2 Å	2.838 Å
H_2O_{inter}-O_{layer}	2.65 Å	2.68 Å	2.65 Å

* AlC_{inter} refers to the alkaline interlayer counterion, which is K^+ for acid birnessite and Na^+ for the other samples. Inter-atomic distances from interlayer species to O_{layer} are calculated with respect to a unique layer, without adjacent layer whose actual position is unknown as a result of the turbostratic stacking.

Biogenic oxide

As noted above, X-ray scattering from bacterial cells does not produce any significant modulations of the diffracted intensity over the analyzed angular range (Fig. 1d) and, consequently, all experimental features were interpreted as arising from the manganate admixture. As compared to the two previous samples, this oxide has an even lower Mn oxidation state (3.90 ± 0.05, Table 1), thus suggesting a higher content of interlayer Mn, and possibly also of octahedral vacancies. Also, this sample has a lower alkali/Mn ratio (0.167 ± 0.003), which suggests a higher proportion of vacant layer sites capped by interlayer Mn. Accordingly, the optimum fit to the XRD pattern of this oxide (Fig. 3c; R_{WP} = 9.8%, R_{EXP} = 3.1%) was obtained for the following

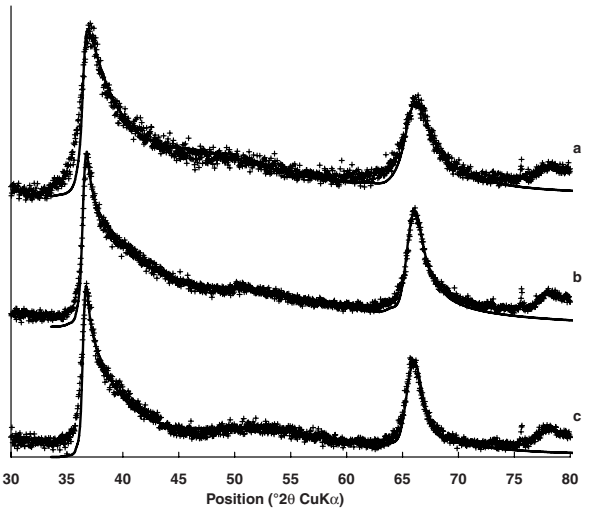

FIGURE 3. Comparison between experimental and calculated XRD patterns for the various Mn oxide samples. Patterns as for Figure 2. Structural parameters used for calculations are listed in Tables 2 and 3. Calculations are performed for the 20,11 and for the 02,31 bands (maxima at ~37 and 66 °2θ Cu*K*α, respectively). (**a**) δ-MnO_2, (**b**) acid birnessite, (**c**) biogenic oxide.

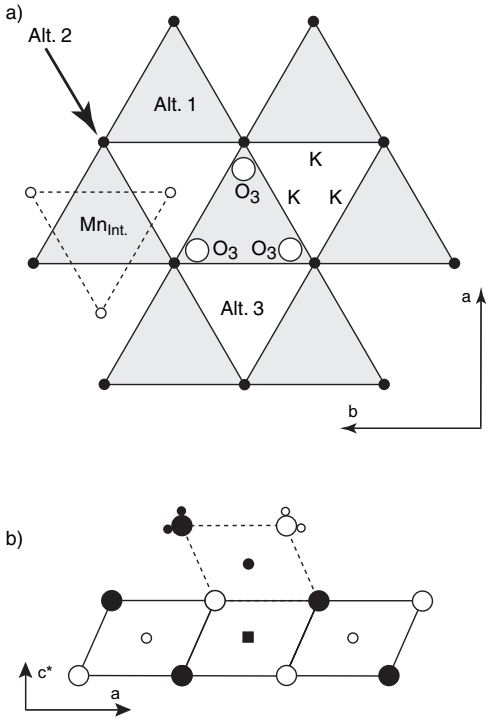

FIGURE 4. Structure model for the various Mn oxide samples. (**a**) Projection on the **a-b** plane. The upper surface of the layer is shown as light shaded triangles. O_{layer} atoms of this upper surface are shown as solid circles, whereas Mn_{layer} atoms are not shown. Large open circles represent Na^+ cations and H_2O molecules in δ-MnO_2 [(0.225, 0.0, 0.5)—Position O3]. K represents the position of interlayer K^+ cations in the acid birnessite sample. Positions labeled Alt *n* (*n* = 1, 2, 3) represent test positions to assess the sensitivity of calculated XRD patterns to the position of interlayer species. The dashed triangle outlines the upper surface of the $Mn_{interlayer}$ coordination octahedron, which is defined by three $H_2O_{interlayer}$ (small open circles). (**b**) Projection along the **b** axis. Open and solid symbols indicate atoms at $y = 0$ and $y = \pm ½$, respectively. Large circles represent O_{layer} atoms, small circles represent Mn atoms. The solid square represents a vacant layer site. The dashed line outlines the $Mn_{interlayer}$ coordination octahedron, which is defined by O_{layer} and $H_2O_{interlayer}$.

structural formula:

$$H_aNa_{0.15}(H_2O)_{0.45}Mn^{2+}_{0.167}{}^{3+}_{}(H_2O)_{0.50}[Mn^{4+}_{0.833},\square_{0.167}]O_2 \quad (4)$$

The amounts of vacancies and interlayer Mn are identical (0.167 per octahedron), and the same as in HBi (Lanson et al. 2000). However, the short <Mn-O_{layer}> distance (1.92 Å, Table 4) pleads for the sole presence of Mn^{4+} within the octahedral layers in contrast to HBi. In the optimized structural model, octahedrally coordinated interlayer Mn atoms are slightly farther from the layer surface (*z*-coordinate = 2.15 Å, Table 3 c) than in HBi (*z*-coordinate = 2.10 Å; Lanson et al. 2000). This position results in a <$Mn_{interlayer}$-O_{layer}> distance of 2.00 Å, that is significantly longer than usual (1.98 Å). This increase in distance is consistent with the likely presence of interlayer divalent Mn cations in the biogenic oxide. The residual layer charge is balanced by interlayer Na^+ cations (0.15 per octahedron) and protons, the amount of which depends on the actual valency of interlayer Mn cations. The amount of interlayer Na estimated from our XRD model is consistent with the Na/Mn molar ratio (0.167 ± 0.003) reported by Villalobos et al. (2003), and the amount of water bound to Na (8.2%) is slightly smaller than the TGA value (10.0%). Finally, the optimized atomic coordinates for Na and H_2O are similar to those obtained for δ-MnO_2, leading again to meaningful <H_2O-O_{layer}> and <Na-O_{layer}> distances.

Sensitivity of calculated XRD patterns to structural parameters. As the optimum fits to the experimental data were obtained using a trial-and-error approach (making the assessment of uncertainties very difficult), the actual sensitivity of the XRD simulations to key structural parameters needs to be assessed. The sensitivity to the position of interlayer species will be illustrated by taking δ-MnO_2 as a case study. The optimum positions of Na and H_2O [(0.225, 0.0, 0.5) and equivalent positions] are labeled "O3" in Figure 4. Placing the two interlayer species above or below an empty layer octahedron [position (0.0, 0.0, 0.5), Alt. 1 in Fig. 4] modified the XRD profile considerably, especially the 20,11 band (Fig. 5a, R_{WP} = 21.9%). Even a small shift of these "light" species from their optimum (0.225, 0.0, 0.5) position to (0.333, 0.0, 0.5) (position Alt. 2 in Fig. 4) changed significantly the calculated XRD profile relative to the best simulation (Fig. 5b, R_{WP} = 12.2%). Finally, when interlayer species are sitting above/below the tridentate cavities [Position Alt. 3 in Fig. 4 with

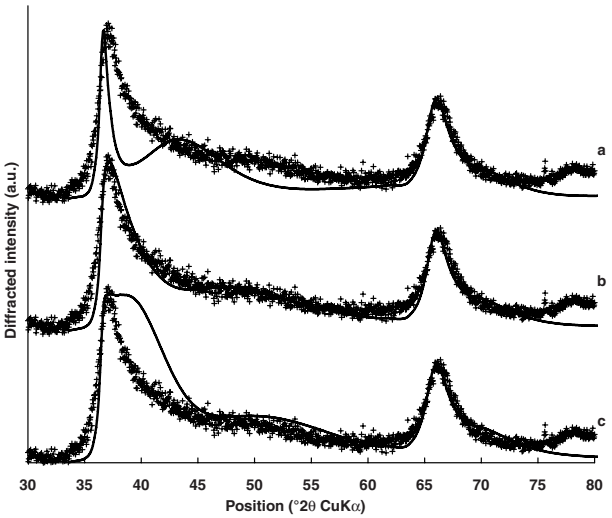

FIGURE 5. Comparison between experimental and calculated XRD patterns for δ-MnO_2. Patterns as for Figure 2. Structural parameters used for calculations are listed in Tables 2 and 3a. Calculations are performed for the 20*l*,11*l* and for the 02*l*,31*l* sets of reflections (maxima at ~37 and 66 °2θ Cu*K*α, respectively). (**a**) Interlayer Na^+ cations and H_2O molecules are located above or below layer octahedra [position (0.0, 0.0, 0.5)—Alt. 1 in Fig. 4] rather than in the optimum O3 position (0.225, 0.0, 0.5) (Fig. 3a). (**b**) Interlayer Na^+ cations and H_2O molecules are located in (0.333, 0.0, 0.5) (position Alt. 2 in Fig. 4) rather than in the optimum O3 position (0.225, 0.0, 0.5). (**c**) Interlayer Na^+ cations and H_2O molecules are located above/below the tridentate cavities at the layer surface [Position Alt. 3 in Fig. 4 with coordinates (–0.333, 0.0, 0.5)] rather than in the optimum O3 position (0.225, 0.0, 0.5).

coordinates (–0.167, 0.0, 0.5)], the calculated 20,11 band was broadened, and differed greatly from experimental data (Fig. 5c, R_{WP} = 24.1%).

Figure 6 illustrates the sensitivity of the calculated XRD profiles to the mean radial dimension of the CSDs in the **a-b** plane, taking again δ-MnO_2 as an example. In Figure 6a, this dimension has been increased from 6.0 nm, the optimum value (Table 2), to 10.0 nm. As a result, the 20,11 band peaks at lower 2θ value. In addition, the calculated band is sharper, leading to a poorer reproduction of the experimental profile (R_{WP} = 15.0%). An opposite effect is observed when the mean CSD radial dimension is decreased from 6.0 to 3.0 nm (Fig. 6b, R_{WP} = 11.6%). Note that the CSD size does not affect the position of the modulation at about 45 °2θ Cu*K*α, which depends only on the layer structure.

The sensitivity of the calculated XRD profiles to the location and amount of interlayer Mn is illustrated next with the biogenic oxide (Fig. 7). Decreasing the stoichiometric coefficient tc (Eq. 1) from its optimum 0.167 value to 0.100 modified the shape of the high-angle "tail" of the 20,11 band in a manner that smoothened the scattering dip at ~45 °2θ Cu*K*α rendering the calculated hump less pronounced (Fig. 7a, R_{WP} = 11.3%) relative to the optimum fit (Fig. 3c, R_{WP} = 9.8%). When both the proportion of interlayer Mn and layer vacancies were decreased from 0.167 to 0.100, the lineshape of the 20,11 band was broadened (Fig. 7b, R_{WP} = 14.6%). As expected from the high sensitivity of the calculated XRD patterns to the position of "light" interlayer species, demonstrated previously with Na and H_2O in δ-MnO_2, moving interlayer Mn from its optimal position dramatically modified the 20,11 lineshape, as observed when the 0.167 interlayer Mn atoms were located above/below the tridentate cavities (position Alt. 3 in Fig. 4; Fig. 7c, R_{WP} = 25.3%).

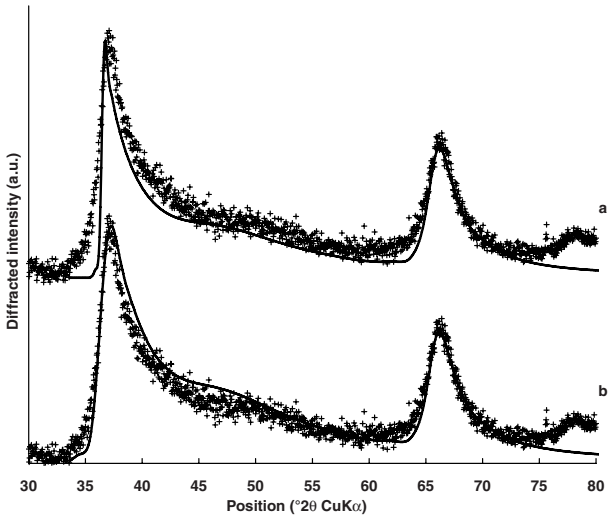

FIGURE 6. Comparison between experimental and calculated XRD patterns for δ-MnO_2. Patterns as for Figure 2. Structural parameters used for calculations are listed in Tables 2 and 3a. Calculations are performed for the 20*l*,11*l* and for the 02*l*,31*l* sets of reflections (maxima at ~37 and 66 °2θ Cu*K*α, respectively). (**a**) Mean radial dimension of the CSD in the **a-b** plane is increased from the optimum 6.0 (Fig. 3a) to 10.0 nm. (**b**) Mean radial dimension of the CSD in the **a-b** plane is decreased from the optimum 6.0 to 3.0 nm.

EXAFS spectra

The k^3-weighted Mn *K*-edge EXAFS spectra collected for the samples are shown in Figure 8a. Frequencies for all the Mn oxides studied were similar, with differences between the samples arising mostly in the amplitudes. These amplitude differences are also evident in the corresponding radial structure functions (RSFs, uncorrected for phase shifts) shown in Figure 8b. The uncleaned biogenic oxide sample shows a somewhat distinctive behavior in the 3–8 $Å^{-1}$ interval (Fig. 8a). These effects are probably a contribution of a relatively important Mn^{2+} fraction (16–19 mol%) in this sample, which is absent from the others (Villalobos et al. 2003).

The RSFs exhibit two principal peaks at similar interatomic distances for all samples (Fig. 8b), including the uncleaned biogenic oxide. From a qualitative comparison with previously reported spectra for layer type Mn oxides, it can be concluded that these two peaks arise mainly from single-scattering photoelectron interactions in the first Mn-O shell and in the second Mn-Mn shell, respectively (Manceau and Combes 1988; Manceau et al. 1992; Silvester et al. 1997). Differences among the samples are observed mostly in the peak amplitudes, particularly for the Mn-Mn peak, and in the small feature that appears just beyond this peak at $R + \Delta R$ ~3 Å. This feature was used to elucidate important structural differences between the Mn oxides using single-scat-

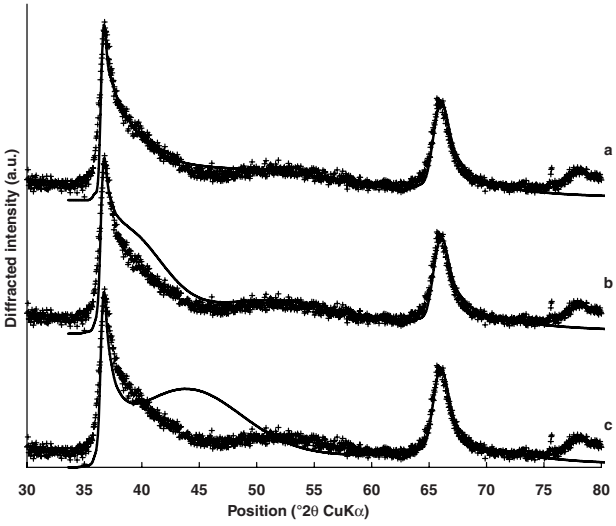

FIGURE 7. Comparison between experimental and calculated XRD patterns for the biogenic oxide. Patterns as for Figure 2. Structural parameters used for calculations are listed in Tables 2 and 3c. Calculations are performed for the 20*l*,11*l* and for the 02*l*,31*l* sets of reflections (maxima at ~37 and 66 °2θ Cu*K*α, respectively). (**a**) Amounts of vacant layer sites and of interlayer Mn cations are assumed to be 0.167 and 0.100, as compared to the optimum 0.167 and 0.167 values (Fig. 3c), respectively. (**b**) Amounts of vacant layer sites and of interlayer Mn cations are assumed to be 0.100 and 0.100, as compared to the optimum 0.167 and 0.167 values, respectively. (**c**) Interlayer Mn cations are located above/below the tridentate cavities at the layer surface [Position Alt. 3 in Fig. 4 with coordinates (–0.333, 0.0, 0.299)] rather than in the optimum position (0.0, 0.0, 0.299).

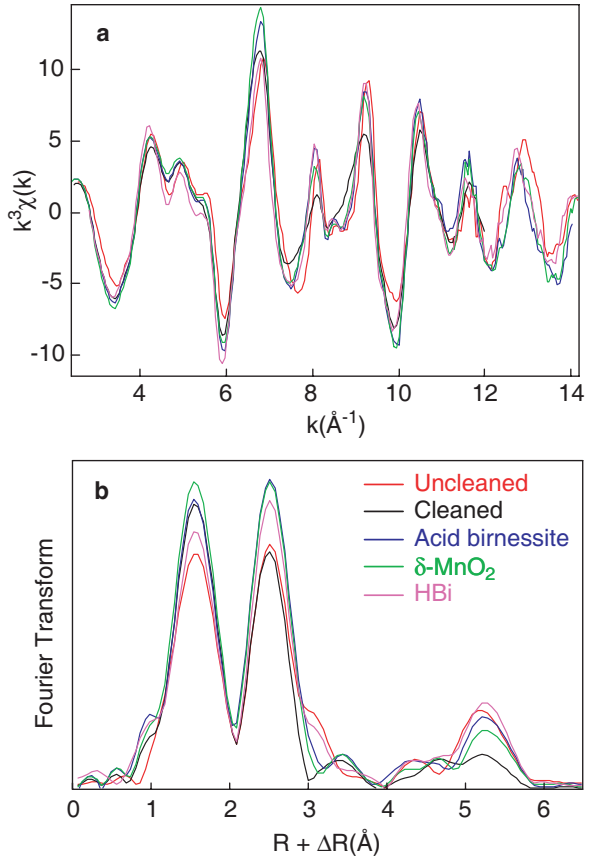

FIGURE 8. (**a**) k^3-weighted Mn *K*-edge EXAFS spectra of Mn oxides lacking 3D ordering and of H-birnessite. (**b**) Magnitude of the Fourier transform (uncorrected for phase shifts).

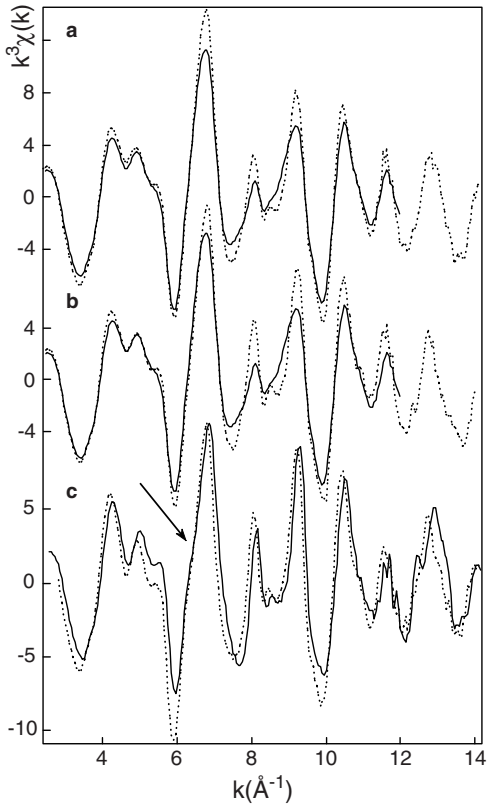

FIGURE 9. Comparison between k^3-weighted Mn *K*-edge EXAFS spectra of (**a**) the cleaned biogenic Mn oxide and δ-MnO$_2$, (**b**) the cleaned biogenic Mn oxide and acid birnessite, and (**c**) the uncleaned biogenic Mn oxide and H-birnessite. The arrow denotes the area where the biogenic oxide and H-birnessite overlap (Manceau et al. 1997). Solid lines represent the biogenic samples.

tering ab initio FEFF simulations. Specifically, the presence of a shoulder or a distinctive peak at $R + \Delta R$ ~3 Å for the uncleaned biogenic oxide may be indicative of Mn octahedra in different configurations from the edge-sharing octahedra in the layers, e.g., triple-corner (TC) sharing octahedra, as observed in HBi and chalcophanite (Silvester et al. 1997), and in tectomanganates (Manceau and Combes 1988).

The EXAFS spectrum of the clean biogenic oxide clearly shows a modification of the shape of the second oscillation in the 6–7 Å^{-1} interval (Fig. 8a.), which manifests itself in the disappearance of the feature at $R + \Delta R$ ~3 Å in real space (Fig. 8b). The new shape is very similar to that seen in the spectra and RSFs of δ-MnO$_2$ and acid birnessite (Figs. 9, 10). In contrast, the spectrum for the unclean biogenic sample shows a strong similarity to that for HBi, especially in the region between 6 and 7 Å^{-1} (Fig. 9c) and at $R + \Delta R$ ~3 Å (Fig. 10c, feature C). Therefore, qualitatively, one may conclude that the biogenic sample as it is synthesized by the bacteria most likely contains interlayer Mn, in similar configuration to HBi.

The peak caused by the third Mn layer shell at $R + \Delta R$ ~5.2 Å (Fig. 10c, feature D) is more intense than the peak of the second Mn layer shell at $R + \Delta R$ ~4.5 Å, although the two shells comprise six Mn atoms. The magnification of peak D has been attributed to a "focusing effect" between aligned cations in layer type metal oxides (O'Day et al. 1994).

Simulations of the EXAFS spectra

δ-MnO$_2$. This layer Mn oxide appears to have a simple structure arising from the homogeneity of its Mn oxidation state (Villalobos et al. 2003). The FEFF simulations of the $k^3\chi(k)$ data filtered in the $1.0 < R + \Delta R < 3.2$ Å interval are shown in Figure 11 and the corresponding optimized parameters are listed in Table 5. The first two shells correspond to Mn-O and Mn-Mn distances of 1.90 Å and 2.88 Å, respectively. The edge-sharing configuration of the Mn^{4+} octahedra (six shared edges per octahedron) is isostructural with that in bivalent metal hydroxides of the brucite [Mg(OH)$_2$] group, including pyrochroite [Mn(OH)$_2$]. To reconcile the interatomic distances obtained by FEFF simulation with this configuration in a crystallographic model, the Mn^{4+} octahedra must flatten slightly. To ensure a Mn-Mn distance of 2.88 Å between adjacent octahedra while keeping all Mn-O distances equal to 1.90 Å, the O-O distance along shared edges must shorten to 2.48 Å (Fig. 12, inset). The O-O distances along the unshared edges in this configuration are effectively equal to the interatomic Mn-Mn distance of 2.88 Å.

An idealized octahedral sheet for δ-MnO$_2$ may now be

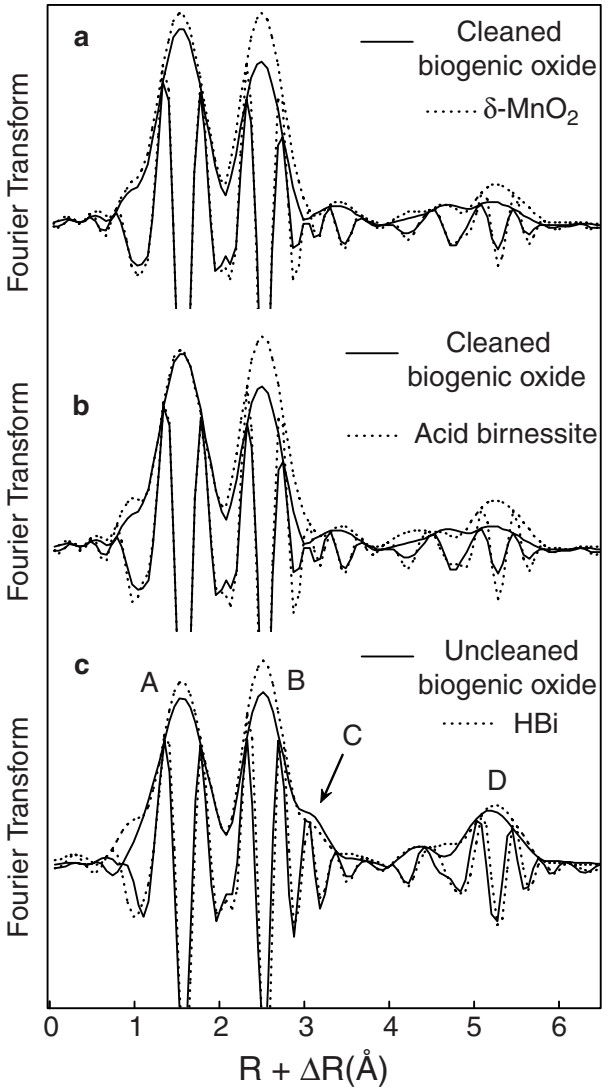

FIGURE 10. Comparison between the magnitude and imaginary part of the Fourier transforms (uncorrected for phase shifts) for (**a**) the cleaned biogenic Mn oxide and δ-MnO_2, (**b**) the cleaned biogenic Mn oxide and acid birnessite, and (**c**) the uncleaned biogenic Mn oxide and H-birnessite. The letters refer to the four different shells identified. A indicates the peak due to Mn-O1 distance, B to the Mn-Mn1 distance, C mostly to the Mn-Mn(tc) distance, and D to the third Mn layer shell distance. The latter was not modeled with the single scattering model employed in the spectral simulations. The arrow denotes the area where the biogenic oxide and H-birnessite overlap (Manceau et al. 1997).

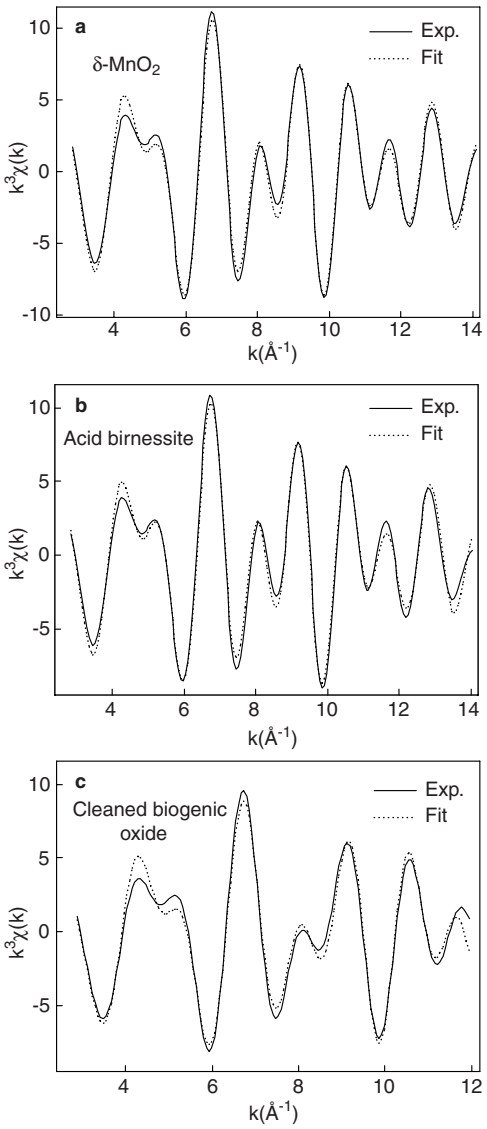

FIGURE 11. Fourier-filtered experimental EXAFS spectra and FEFF simulations of the $1.0 < R + \Delta R < 3.2$ Å region for (**a**) δ-MnO_2, (**b**) acid birnessite, (**c**) NaOCl-cleaned biogenic Mn oxide, according to the parameters listed in Table 5.

constructed (Fig. 12) in which all Mn near neighbor distances are determined by geometry alone. For example, a second O shell (O2) is expected at 3.45 Å, and further Mn layer shells are expected at 4.99 Å (dotted lines in Fig. 12) and 5.76 Å. The O2 shell at 3.45 Å from Mn is within the range of influence of the edge-sharing Mn shell (Mn1), and of the triple-corner sharing Mn shell [Mn(tc)], when present, and, consequently, it was included in the spectral fits for all sample spectra. However, spectral simulations showed that adding the Mn-O2 electronic wave improves the fit in the 4–6 $Å^{-1}$ k interval, but does not modify significantly

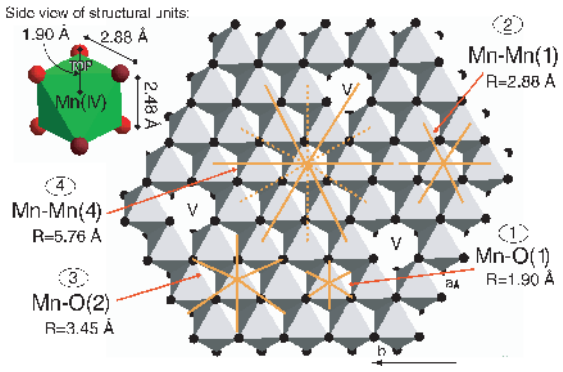

FIGURE 12. Idealized hexagonal layer structure of edge-sharing Mn^{4+}-O_6 octahedra (inset at left) for δ-MnO_2.

the EXAFS parameters from the Mn1 and Mn(tc) shells because these shells have a maximum amplitude at higher k (Manceau and Combes 1988; Schlegel et al. 2001).

According to the ideal hexagonal layer model of δ-MnO_2, and in the absence of configurations other than edge-sharing octahedra, six near neighbors of Mn centers are expected for all shells (Fig. 12). The optimized fit for the O1 shell indeed yielded N very close to 6 (Table 5). However, the Mn1 shell fit produced a considerably lower value of N, even when taking into account the commonly accepted precision of 20% in this parameter. Two factors may predominate in causing this reduction: vacant cation sites (i.e., the absence of some Mn near neighbors per Mn center present) and the contribution of particle-edge octahedra that have an incomplete shell of near neighbors, a contribution that is important because of the small size of the layers in our samples.

Based on a Mn-Mn1 distance of 2.88 Å as obtained from analysis of the first Mn shell (Table 5), and on a layer size estimate from our XRD simulations of δ-MnO_2 (from the coherent scattering domain radial dimensions, Table 2), a rough estimate of the contribution of layer-edge octahedra may be performed: one sheet of a square particle of dimensions 85 × 85 $Å^2$ yields a total of $(85/2.88)^2 \sim 900$ octahedra, of which $4 \times (85/2.88) \sim 120$ occur at the edges. The latter represents 13% of the total. Assuming smooth edges, we estimate that ca. 4 Mn near-neighbors occur for every edge octahedron (Fig. 12). Thus the average number of nearest Mn neighbors for all Mn atom centers in the 85×85 $Å^2$ particle is about $0.13 \times 4 + (1 - 0.13) \times 6 = 5.74$; i.e., a reduction of less than 5% from the ideal value. Therefore, the low coordination number (28% difference) observed by EXAFS spectral fitting must be due primarily to the presence of vacant Mn sites. Unfortunately, the uncertainty of the predicted N value by EXAFS is too high to render a useful quantitative estimate of the vacancy content by this method. However, it provides a convincing qualitative explanation for the occurrence of Mn N values significantly lower than the theoretical value of 6.

HBi with an enhanced 3D ordering. The HBi studied by Silvester et al. (1997) has a more complex structure than δ-MnO_2 because of the presence of significant Mn^{3+} in the layer and at interlayer sites in TC configuration above cation vacancies. The significant increase by 0.01 Å of the Mn-Mn1 distance relative to δ-MnO_2 (Table 5) is indicative of the presence of Mn^{3+} in the layer, whereas the Mn shell at 3.49 Å with an effective coordination number of 2.8 is characteristic of corner-sharing linkages between layer and interlayer octahedra.

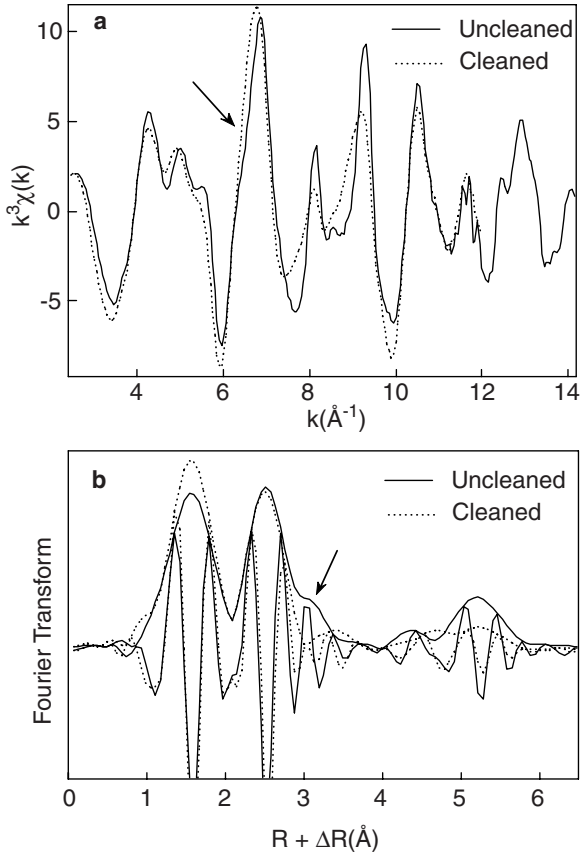

FIGURE 13. Comparison between the EXAFS data of the cleaned and uncleaned biogenic Mn oxide. (**a**) k^3-weighted Mn K-edge EXAFS spectra. (**b**) Magnitude and imaginary part of the Fourier transforms (uncorrected for phase shifts).

Acid birnessite. As expected from the average Mn oxidation number of 3.96 for this oxide (Villalobos et al. 2003) and from the RSF (Fig. 8b) and XRD data, FEFF simulations gave optimized structural parameters very similar to those for δ-MnO_2 (Fig. 11b, Table 5). The main difference between the two structures lies in the larger size of the diffracting crystallites (CSD) in acid birnessite.

Biogenic oxide. Simulation of the NaOCl-cleaned sample of the biogenic oxide produced shells and optimized structural

TABLE 5. Optimized simulation parameters of K-edge Mn EXAFS for biogenic Mn oxide and synthetic analogs

Sample	Shells†												
	Mn-O1			Mn-O2‡			Mn-Mn1			Mn-Mn(tc)			Δ*E*
	R (Å)	*N*	σ² (Å²)	R (Å)	*N*	σ² (Å²)	R (Å)	*N*	σ² (Å²)	R (Å)	*N*	σ² (Å²)	
δ-MnO_2	1.90	5.7	0.0042	3.49	6*	0.0167	2.88	4.3	0.0042	–	–	–	0.6
Acid birnessite	1.90	5.3	0.0038	3.50	6*	0.0134	2.88	4.6	0.0045	–	–	–	0.8
H-birnessite	1.91	4.5	0.0032	3.61	6*	0.0049	2.89	4.8	0.0051§	3.49	2.8	0.0051§	1.6
Biogenic (clean)	1.90	5.1	0.0035	3.42	6*	0.0149	2.87	2.9	0.0033	–	–	–	–0.4
Biogenic (unclean)	1.91	4.8	0.0030	3.61	6*	0.0049	2.87	4.8	0.0051§	3.49	2.8	0.0051§	3.6
λ-MnO_2 (standard)	1.91	6.0	0.0025	3.52	6*	0.0088	2.85	6.0	0.0028				1.5

* Fixed value in the optimization procedure.
† S_0^2 values used for the amplitude normalization were 0.73 for the O1 shell and 0.80 for the Mn shells. Typical uncertainty on Mn-O1, Mn-Mn1, and Mn-Mn(tc) interatomic distances and coordination numbers are 0.02 Å and ± 1.5, respectively.
‡ The Mn-O2 shell contribution is very weak and thus a high correlation occurs between the optimized frequency and Δ*E*, resulting in a low precision of the predicted parameters.
§ σ values for the Mn1 and Mn(tc) shells were floated but kept identical.

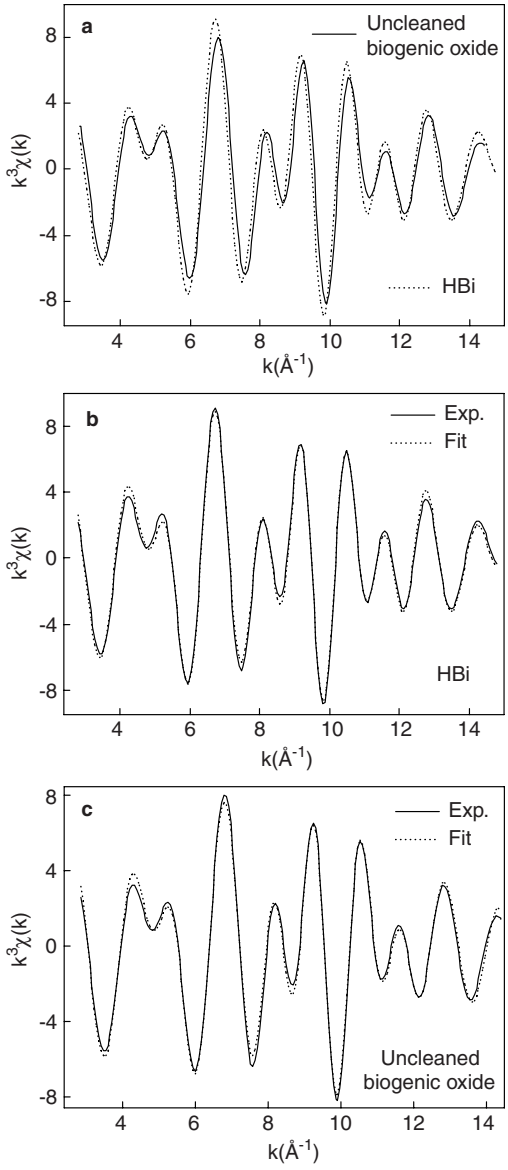

FIGURE 14. Fourier-filtered experimental EXAFS spectra of the 1.0 < R + ΔR < 3.2 Å region for HBi and the uncleaned biogenic oxide (**a**), and FEFF simulations according to the parameters listed in Table 5 (**b-c**).

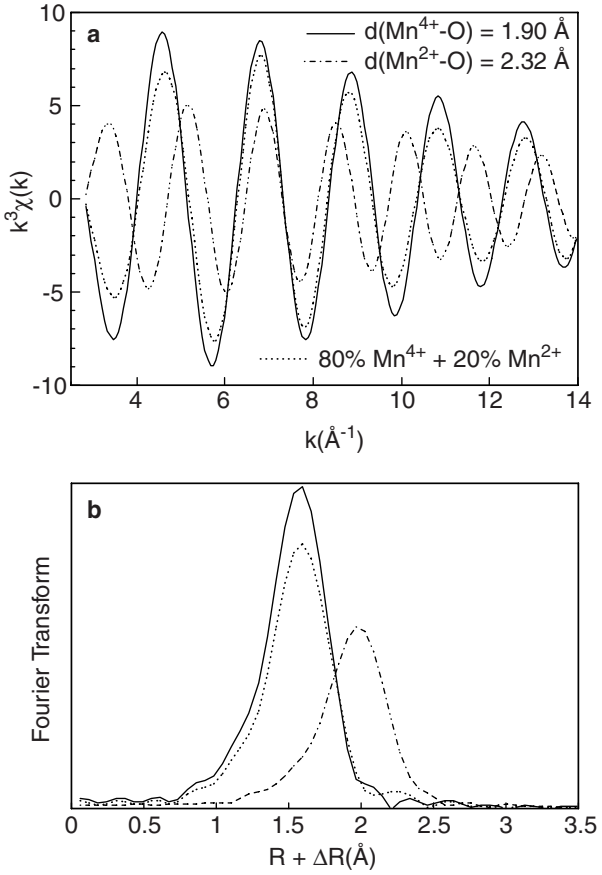

FIGURE 15. EXAFS contribution (**a**) and magnitude of the Fourier transform (**b**) for a theoretical Mn oxide composed of 80% Mn^{4+} and of 20% Mn^{2+}. Despite the widely differing $\chi(k)$ frequencies of the Mn^{4+}-O and Mn^{2+}-O waves, the Fourier transform of the mixture differs from that of a pure Mn^{4+} compound only by its amplitude.

parameters different from the uncleaned sample (Fig. 13), but very similar to those of δ-MnO_2 and acid birnessite (Fig. 11c; Table 5). Figures 9c and 14a show that HBi has a higher wave frequency than the unclean biogenic oxide, which translates in real space to a shift to higher $R + \Delta R$ values of peaks B and D (Fig. 10c). Accordingly, Table 5 shows that the Mn-Mn1 distance is greater by 0.02 Å in HBi. This is due to the presence of layer Mn^{3+} in the latter, and its absence in the biogenic oxide. Matching the simulation of HBi (Fig. 14b), the prominent shoulder at ~3 Å in the RSF of the uncleaned sample (peak C in Fig. 10c) was successfully simulated with a TC Mn shell at 3.49 Å (Fig. 14c, Table 5). The oxidation state of this interlayer Mn species is different in the biogenic oxide (Mn^{2+}) from that in HBi (Mn^{3+}), however, the Mn-Mn(tc) EXAFS distance is the same for both (Table 5). This may be explained as a trade-off between the larger radius of Mn^{2+} compared to Mn^{3+}, and the need for Mn^{2+} to approach the layer at a closer distance to compensate for a similar negative layer charge. This type of behavior has been reported in chalcophanite, in which Zn is octahedrally coordinated, but has Zn-O_{layer} distances characteristic of a tetrahedral coordination owing to the lowering of the Zn position in the direction of the layer (Wadsley 1955).

Additionally, note that the O1 shells of the uncleaned sample and HBi have lower *N* values than the other samples (Table 5). This difference occurs because the high proportion of low-valent Mn in the two samples causes a higher disorder in the Mn-O EXAFS frequency, manifested in a decrease from what would be observed for pure Mn^{4+}-O pairs. This situation is illustrated in Figure 15, which shows an EXAFS simulation for a hypothetical system consisting of 80% Mn^{4+}-O and 20% Mn^{2+}-O pairs. In such a system, the frequency of the shorter Mn^{4+}-O pair dominates the EXAFS spectrum (Fig. 15a) and, therefore, the RSF peak for the composite Mn valency spectrum appears at the same distance as that for the pure Mn^{4+} spectrum, but with a lower amplitude (Fig. 15b).

General discussion

Ability of the trial-and-error XRD modeling approach to determine the structure of turbostratic compounds. The ability of the trial-and-error approach used in the present study to unravel the structure of defect-bearing compounds has been amply demonstrated in recent studies of different birnessite varieties with an enhanced 3D ordering (Manceau et al. 1997; Drits et al. 1998a; Lanson et al. 2000, 2002a, 2002b; Gaillot et al. 2003, 2004). Based on the above fits to the experimental data and the subsequent sensitivity analysis, it is clear that this trial-and-error approach can also be applied to build meaningful structure models for extremely defective (turbostratic stacking—100% of random stacking faults) layered compounds. The symmetry and cation occupancy of the octahedral layer, and to some extent the amounts and positions of interlayer species, were well constrained. Specifically, it was possible to assess the presence and the number of interlayer Mn cations associated with vacant layer sites, and to determine their position with a reasonable precision (e.g., Figs. 3c and 7). The position and, to a lesser extent, the amount of "light" interlayer species, such as Na^+ and H_2O molecules, were also obtained by this approach (e.g., Figs. 3a and 5). The initial hypothesis of the amount of interlayer H_2O being three times the amount of interlayer alkali cations proved to be essentially correct when compared to the water contents determined from TGA measurements. However, because of the contrasting affinity of K^+ and Na^+ cations for H_2O, the amount of H_2O determined from XRD profile modeling is underestimated for Na-bearing birnessite varieties (δ-MnO_2 and biogenic birnessite), whereas it is overestimated for K-bearing birnessite (acid birnessite). Our modeling procedure also provided estimates of the CSD sizes in the **a-b** plane for these compounds (e.g., Figs. 3a and 6).

The high sensitivity of XRD profiles to the structure of highly defective phyllomanganates contrasts with the limited sensitivity reported previously for smectites. For example, Manceau et al. (2000a, 2000b) used a similar modeling approach to determine average cation occupancy in nontronite for which the layer and interlayer structures were reasonably well known, a few parameters being left to refine. For this purpose these authors used the relative intensities of the 02,11 and 20,13 bands because no modulations were observed for the two diffraction bands. In the present study, we showed that the position and profile of the bands of turbostratic phyllomanganates depend on the amount and atomic coordinates of both layer and interlayer species, and thus they can be used for structural chemistry determination. However, similar modulations can result from the partial ordering of the layer stacking (e.g., Ben Brahim et al. 1983, 1984; Drits and Tchoubar 1990; Viani et al. 2002). Special attention should thus be paid to the structural interpretation of these modulations, and, in this respect, verifying the structural XRD model with independent data from another structural technique, such as EXAFS spectroscopy, is always warranted.

Particle size considerations. The small coherent scattering dimensions obtained from XRD simulations provided estimates for the size of the diffracting crystallites in the nanometer range. The implications of this small particle size include the exposure at the surface of a large proportion of the total structure. Therefore, edge surface sites, which contain unsaturated singly and doubly coordinated oxygen groups (Fig. 12), are expected to hold a relatively high proportion of the total particle charge and thus contribute palpably to ion sorption capacity. Other implications of small particle size may be relevant not only to reactivity studies, but also to structural characterization using wet-chemistry and spectroscopic techniques, such as those employed by Villalobos et al. (2003). For example, the molar ratio, [Mn(IV) + vacancies]/O is no longer expected to be 0.5, as in infinitely large octahedral layers. Small particle size in the radial direction has the potential to create "border effects" that may influence characterization based on spectroscopic techniques that have been calibrated using samples having much larger particle size.

Comparisons between Mn oxides studied. Complementary information obtained from simulations of XRD patterns and Mn *K*-edge EXAFS spectra has led to more accurate determination of the structures of the biogenic Mn oxide and its two synthetic analogs investigated by Villalobos et al. (2003). Hexagonal layer symmetry was established for all three Mn oxides studied, with differences occurring mainly in the number of layer vacancies, in the cation interlayer content, and in particle size (coherent scattering domain radial dimensions and number of randomly stacked sheets per crystallite). The uncleaned sample of the biogenic Mn oxide is structurally related to synthetic HBi, including similar vacancy contents and the presence of low-valency interlayer Mn in TC configuration. However, the biogenic phase's octahedral layer is composed of tetravalent Mn only, in contrast to HBi, but in close similarity with δ-MnO_2 and acid birnessite. Thus, the layer charge originates only from the presence of vacant layer sites. Another characteristic of the biogenic oxide is the presence of Mn^{2+} in the interlayer, whereas HBi has essentially Mn^{3+}, and δ-MnO_2 and acid birnessite have no Mn^{2+}. This Mn^{2+} is most likely a remnant of unoxidized Mn^{2+} added to the system initially. A recent X-ray absorption study of the oxidation product of a *Leptothrix* bacterium (Jurgensen et al. 2004) detected both Mn^{2+} and Mn^{3+}in the birnessite-like biogenic oxide, suggesting that Mn^{3+} may be a structural component of certain biogenic oxides. In yet another study on biogenic oxides, Mn^{3+} was detected by Scanning Transmission X-ray Microscopy (STXM) (Pecher et al. 2003; Toner et al. 2004), but this species was assigned an intermediate role in the bacterial oxidation process to Mn^{4+}.

ACKNOWLEDGMENTS

The first author thanks Philip N. Ross (Materials Science Divison, Lawrence Berkeley National Laboratory) for use of a TGA-DTA apparatus and John Bargar for facilitating EXAFS measurements and providing technical assistance at the beamline. The third author expresses gratitude to the Division of Ecosystem Sciences, University of California at Berkeley, for its hospitality during a sabbatical leave visit. This research was funded in part (M.V., B.T., G.S.) by the National Science Foundation, Collaborative Research Activities in Environmental Molecular Science (CRAEMS) program (CHE-0089208), in part (B.L.) by the ACI/FNS ECCO (EcoDyn) program in France, and in part (A. M.) by a LDRD grant through the Advanced Light Source, Lawrence Berkeley National Laboratory. SSRL is a national user facility operated on behalf of the U.S. DOE, Office of Basic Energy Sciences.

REFERENCES CITED

Bartlett, R.J. and James, B.R. (1993) Redox chemistry of soils. Advances in Agronomy, 50, 151–208.

Ben Brahim, J., Besson, G., and Tchoubar, C. (1983) Layer succession and water molecules arrangement in a homogeneous two-water layer Na-smectite. In J. Konta, Ed., 5th Meeting of the European Clay Groups, p. 65–75. Univerzita Karlova, Prague.

——— (1984) Etude des profils des bandes de diffraction X d'une beidellite-Na hydratée à deux couches d'eau. Détermination du mode d'empilement des feuillets et des sites occupés par l'eau. Journal of Applied Crystallography, 17, 179–188.

Bilinski, H., Giovanoli, R., Usui, A., and Hanzel, D. (2002). Characterization of Mn oxides in cemented streambed crusts from Pinal Creek, Arizona, U.S.A., and in hot-spring deposits from Yuno-Taki Falls, Hokkaido, Japan. American Mineralogist, 87, 580–591.

Brindley, G.W. (1980) Order-disorder in clay mineral structures. In G.W. Brindley, and G. Brown, Eds. Crystal Structures of Clay Minerals and their X-ray Identification, p. 125-195. Mineralogical Society, London.

Catts, J.G. and Langmuir, D. (1986). Adsorption of Cu, Pb, and Zn by delta-MnO2: applicability of the site binding-surface complexation model. Applied Geochemistry, 1, 255–264.

Ching, S., Krukowska, K.S., and Suib, S.L. (1999) A new synthetic route to todorokite-type manganese oxides. Inorganica Chimica Acta 294(2), 123–132.

Chukhrov, F.V., Sakharov, B.A, Gorshkov, A.I., Drits, V.A., and Dikov, Y.P. (1985) Crystal structure of birnessite from the Pacific Ocean. International Geology Review, 27, 1082–1088.

Chukhrov, F.V., Gorshkov, A.I., and Drits, V.A. (1989) Supergenic manganese hydrous oxides, 208 p. Nauka, Moscow.

Drits, V.A. and Tchoubar, C. (1990) X-ray diffraction by disordered lamellar structures: Theory and applications to microdivided silicates and carbons, 371 p. Springer-Verlag, Berlin.

Drits, V.A., Silvester, E., Gorshkov, A.I., and Manceau, A. (1997) Structure of synthetic monoclinic Na-rich birnessite and hexagonal birnessite: I. Results from X-ray diffraction and selected-area electron diffraction. American Mineralogist, 82, 946–961.

Drits, V.A., Lanson, B., Gorshkov, A.I., and Manceau, A. (1998a) Substructure and superstructure of four-layer Ca-exchanged birnessite. American Mineralogist, 83, 97–118.

Drits, V.A., Eberl, D.D., and Srodon, J. (1998b) XRD measurement of mean thickness, thickness distribution and strain for illite and illite-smectite crystallites by the Bertaut-Warren-Averbach technique. Clays and Clay Minerals, 46, 38–50.

Feng, Q., Yokota, Y., Makita, Y., Yanagisawa, K., and Yamasaki, N. (2001) Synthesis of tunnel manganese oxides from layered manganese oxide by hydrothermal soft chemical process with Rb+ as template. High Pressure Research, 20(1–6) Special Issue SI, 33–38.

Friedl, G., Wehrli, B., and Manceau, A. (1997) Solid phases in the cycling of manganese in eutrophic lakes: New insights from EXAFS spectroscopy. Geochimica et Cosmochimica Acta, 61, 275–290.

Gaillot, A.-C., Flot, D., Drits, V.A., Manceau, A., Burghammer, M., and Lanson, B. (2003) Structure of K-rich birnessite obtained by high-temperature decomposition of KMnO4. Part 1. Two-layer polytype from 800 °C experiments. Chemistry of Materials, 15, 4666–4678.

Gaillot, A.-C., Drits, V.A., Plançon, A., and Lanson, B. (2004) Structure of K-rich birnessite obtained by high-temperature decomposition of KMnO4. Part 2. Phase and structural heterogeneities. Chemistry of Materials, 16, 1890–1905.

Ghiorse, W.C. and Ehrlich, H.L. (1992) Microbial biomineralization of iron and manganese. In H.C.W. Skinner and R.W. Fitzpatrick, Eds., Biomineralization Processes. Iron, Manganeso, Catena supplement 21, p. 75–99. Cremlingen-Destedt, Germany.

Golden, D.C., Chen, C.C., and Dixon, J.B. (1987) Transformation of birnessite to buserite, todorokite, and manganite under mild hydrothermal treatment. Clays and Clay Minerals, 35, 271–280.

Gorshkov, A.I., Drits, V.A., Putilita, V.S., Pokrovskaya, E.V., and Sivtsov, A.V. (1992) Natural and synthetic birnessites. Lithology and Raw Materials, 6, 67–81 (in Russian).

Harvey, J.W. and Fuller, C.C. (1998) Effect of enhanced manganese oxidation in the hyporheic zone on basin-scale geochemical mass balance. Water Resources Research, 34, 623–636.

Holland, K.L. and Walker, J.R. (1996) Crystal structure modelling of a highly disordered potassium birnessite. Clays and Clay Minerals, 44, 744–748.

Howard, S.A. and Preston, K.D. (1989) Profile fitting of powder diffraction patterns. In D.L. Bish and J.E. Post, Eds., Modern Powder Diffraction, 20, p. 217–275. Reviews in Mineralogy, Mineralogical Society of America, Chantilly, Virginia.

Jurgensen, A., Widmeyer, J.R., Gordon, R.A., Bendell-Young, L.I., Moore, M.M., and Crozier, E.D. (2004) The structure of the manganese oxide on the sheath of the bacterium Leptothrix discophora: An XAFS study. American Mineralogist, 89, 1110–1118.

Kay, J.T., Conklin, M.H., Fuller, C.C., and O'Day, P.A. (2001) Processes of nickel and cobalt uptake by a manganese oxide forming sediment in Pinal Creek, Globe Mining District, Arizona. Environmental Science and Technology, 35, 4719–4725.

Lanson, B., Drits, V.A., Silvester, E., and Manceau, A. (2000) Structure of H-exchanged hexagonal birnessite and its mechanism of formation from Na-rich monoclinic buserite at low pH. American Mineralogist, 85, 826–838.

Lanson, B., Drits, V.A., Feng, Q., and Manceau, A. (2002a) Structure of synthetic Na-birnessite: Evidence for a triclinic one-layer unit cell. American Mineralogist, 87, 1662–1671.

Lanson, B., Drits, V.A., Gaillot, A.-C., Silvester, E., Plancon, A., and Manceau, A. (2002b) Structure of heavy-metal sorbed birnessite: Part 1. Results from X-ray diffraction. American Mineralogist, 87, 1631–1645.

Luo, J. and Suib, S.L. (1997) Preparative parameters, magnesium effects, and anion effects in the crystallization of birnessites. Journal of Physical Chemistry B, 101, 10403–10413.

Luo, J., Zhang, Q.H., Huang, A.M., Giraldo, O., and Suib, S.L. (1999) Double-aging method for preparation of stabilized Na-buserite and transformations to todorokites incorporated with various metals. Inorganic Chemistry, 38, 6106–6113.

Luo, J., Zhang, Q., and Suib, S.L. (2000) Mechanistic and kinetic studies of crystallization of birnessite. Inorganic Chemistry, 39, 741–747.

Manceau, A. and Combes, J.M. (1988) Structure of Mn and Fe oxides and oxyhydroxides—a topological approach by EXAFS. Physics and Chemistry of Minerals, 15, 283–295.

Manceau, A., Gorshkov, A.I., and Drits, V.A. (1992) Structural Chemistry of Mn, Fe, Co, and Ni in Mn hydrous oxides. II. Information from EXAFS spectroscopy, electron and X-ray diffraction. American Mineralogist, 77, 1144–1157.

Manceau, A., Drits, V.A., Silvester, E., Bartoli, C., and Lanson, B. (1997) Structural mechanism of Co(II) oxidation by the phyllomanganate, Na-buserite. American Mineralogist, 82, 1150–1175.

Manceau, A., Chateigner, D., and Gates, W.P. (1998) Polarized EXAFS, distance-valence least-squares modeling (DVLS), and quantitative texture analysis approaches to the structural refinement of Garfield nontronite. Physics and Chemistry of Minerals, 25, 347–365.

Manceau, A., Lanson, B., Drits, V.A., Chateigner, D., Gates, W.P., Wu, J., Huo, D.F., and Stucki, J.W. (2000a) Oxidation-reduction mechanism of iron in dioctahedral smectites: 1. Crystal chemistry of oxidized reference nontronites. American Mineralogist, 85, 133–152.

Manceau, A., Drits, V.A., Lanson, B., Chateigner, D., Gates, W.P., Wu, J., Huo, D.F., and Stucki, J.W. (2000b) Oxidation-reduction mechanism of iron in dioctahedral smectites: 2. Crystal chemistry of reduced Garfield nontronite. American Mineralogist, 85, 153–172.

Manceau, A., Tamura, N., Celestre, R.S., MacDowell, A.A., Geoffroy, N., Sposito, G., and Padmore, H.A. (2003) Molecular-scale speciation of Zn and Ni in soil ferromanganese nodules from loess soils of the Mississippi basin. Environmental Science and Technology, 37, 75–80.

Manceau, A., Marcus, M.A., Tamura, N., Proux, O., Geoffroy, N., and Lanson, B. (2004) Natural speciation of Zn at the micrometer scale in a clayey soil using X-ray fluorescence, absorption, and diffraction. Geochimica et Cosmochimica Acta, 68, 2467–2483.

Mandernack, K.W., Fogel, M.L., Tebo, B.M., and Usui, A. (1995) Oxygen isotope analyses of chemically and microbially produced manganese oxides and manganates. Geochimica et Cosmochimica Acta, 59, 4409–4425.

Marble, J.C., Corley, T.L., Conklin, M.H., and Fuller, C.C. (1999) Environmental factors affecting oxidation of manganese in Pinal Creek, Arizona. In D.W. Moranwalp and H.T. Buxton, Eds., Water-Resources Investigation Report, p. 173–183. US Geological Survey, West Trenton, New Jersey.

McKenzie, R.M. (1971) The synthesis of birnessite, cryptomelane, and some other oxides and hydroxides of manganese. Mineralalogical Magazine, 38, 493–502.

McKeown, D.A. and Post, J.E. (2001) Characterization of manganese oxide mineralogy in rock varnish and dendrites using X-ray absorption spectroscopy. American Mineralogist, 86, 701–713.

Morgan, J.J. (2000) Manganese in natural waters and earth's crust: Its availability to organisms. In A. Sigel and H. Sigel, Eds., Metal Ions in Biological Systems, 37, p. 1–33. Marcel Dekker, New York.

Nealson, K.H., Tebo, B.M., and Rosson, R.A. (1988) Occurrence and mechanisms of microbial oxidation of manganese. Advances in Applied Microbiology, 33, 279–318.

O'Day, P.A., Rehr, J.J., Zabinsky, S.I., and Brown, G.E. (1994) Extended X-ray absorption fine structure (EXAFS) analysis of disorder and multiple-scattering in complex crystalline solids. Journal of the American Chemical Society, 116, 2938–2949.

Pecher, K., McCubbery, D., Kneedler, E., Rothe, J., Bargar, J., Meigs, G., Cox, L., Nealson, K., and Tonner, B. (2003) Quantitative charge state analysis of manganese biominerals in aqueous suspension using Scanning Transmission X-ray Microscopy (STXM). Geochimica et Cosmochimica Acta, 67, 1089–1098.

Plançon, A. (2002) CALCIPOW—a program for calculating the diffraction by disordered lamellar structures. Journal of Applied Crystallography, 35, 377.

Post, J.E. and Veblen, D.R. (1990) Crystal structure determinations of synthetic sodium, magnesium, and potassium birnessite using TEM and the Rietveld method. American Mineralogist, 75, 477–489.

Post, J.E., Heaney, P.J., and Hanson, J. (2002) Rietveld refinement of a triclinic structure for synthetic Na-birnessite using synchrotron powder diffraction data. Powder Diffraction, 17, 218–221.

Ressler, T. (1998) WinXAS: a program for X-ray absorption spectroscopy data analysis under MS-Windows. Journal of Synchrotron Radiation, 5, 118–122.

Schlegel, M.L., Manceau, A., Charlet, L., Hazemann, J.L. (2001) Adsorption mechanism of Zn on hectorite as a function of time, pH, and ionic strength. American Journal of Science, 301, 798–830.

Shen, Y. F., Zerger, R.P., Deguzman, R.N., Suib, S.L., Mccurdy, L., Potter, D.I., and Oyoug, C.L. (1993) Manganese Oxide Octahedral Molecular Sieves—Preparation, Characterization, and Applications. Science, 260, 511–515.

Silvester, E., Manceau, A., and Drits, V.A. (1997) Structure of synthetic monoclinic Na-rich birnessite and hexagonal birnessite: II. Results from chemical studies and EXAFS spectroscopy. American Mineralogist, 82, 962–978.

Strobel, P., Charenton, J.C., and Lenglet, M. (1987) Structural chemistry of phyllomanganates: Experimental evidence and structural models. Revue de Chimie Minérale, 24, 199–220.

Tebo, B.M. (1991) Manganese(II) oxidation in the suboxic zone of the Black Sea. Deep-Sea Research, 38, S883–S905.

Tebo, B.M. and He, L.M. (1999) Microbially mediated oxidative precipitation reactions. In D.L. Sparks and T.J. Grundl, Eds., Mineral-Water Interfacial Reactions Kinetics and Mechanisms, Chapter 20, p. 393–414. American Chemical Society, Washington, D.C.

Tebo, B.M., Ghiorse, W.C., van Waasbergen, L.G., Siering, P.L., and Caspi, R. (1997) Bacterially mediated mineral formation: Insights into manganese(II) oxidation from molecular genetic and biochemical studies. In J.F. Banfield and K.H. Nealson, Eds., Geomicrobiology: Interactions between microbes and minerals, 35, p. 225–266. Reviews in Mineralogy, Mineralogical Society of America, Chantilly, Virginia.

Thackeray, M.M., de Kock, A., and David, W.I.F. (1993) Synthesis and structural characterization of defect spinels in the lithium-manganese-oxide system. Materials Research Bulletin, 28, 1041–1049.

Tian, Z.R., Yin, Y.G., Suib, S.L., and O'Young, C.L. (1997) Effect of Mg^{2+} ions on the formation of todorokite type manganese oxide octahedral molecular sieves. Chemistry of Materials, 9, 1126–1133.

Tipping, E., Thompson, D.W., and Davison, W. (1984) Oxidation products of Mn(II) in lake waters. Chemical Geology, 44, 359–383.

Toner, B., Fakra, S., Villalobos, M., Warwick, T., and Sposito, G. (2004) Spatially resolved characterization of biogenic manganese oxide production within the biofilm of *Pseudomonas putida* strain MnB1. Applied and Environmental Microbiology 71, 1300-1310.

Viani, A., Gualtieri, A.F., and Artioli, G. (2002) The nature of disorder in montmorillonite by simulation of X-ray diffraction patterns. American Mineralogist, 87, 966–975.

Villalobos, M., Toner, B., Bargar, J., and Sposito, G. (2003) Characterization of the Mn oxide produced by *Pseudomonas putida* strain MnB1. Geochimica et Cosmochimica Acta, 67, 2649–2662.

Wadsley, A.D. (1955) The crystal structure of chalcophanite, $ZnMn_3O_7.3H_2O$. Acta Crystallographica, 8, 1165–1172.

Wehrli, B., Friedl, G., and Manceau, A. (1995) Reaction rates and products of manganese oxidation at the sediment-water interface. In C.P. Huang, C. O'Melia and J.J. Morgan, Eds., Aquatic Chemistry, 244, p. 111–134. Advances in Chemistry Series, American Chemical Society, Washington, D.C.

Zabinsky, S.I., Rehr, J.J., Ankudinov, A., Albers, R.C., and Eller, M.J. (1995) Multiple scattering calculations of X-ray absorption spectra. Physical Reviews, 52, 2995–3009.

MANUSCRIPT RECEIVED FEBRUARY 23, 2005
MANUSCRIPT ACCEPTED NOVEMBER 18, 2005
MANUSCRIPT HANDLED BY JILL PASTERIS